



# Preferential CO oxidation in excess of hydrogen over Au/HMS catalysts modified by Ce, Fe and Ti oxides

T.A. Zepeda<sup>a,\*</sup>, A. Martinez-Hernández<sup>b</sup>, R. Guil-López<sup>c</sup>, B. Pawelec<sup>c</sup>

<sup>a</sup> Centro de Nanociencias y Nanotecnología – UNAM, Km. 107 Carretera Tijuana-Ensenada, CP. 22800, Ensenada, B.C., Mexico

<sup>b</sup> Universidad Autónoma de Nuevo León, Facultad de Ciencias Químicas, Pedro de Alba S/N, Cd. Universitaria C.P. 66400, San Nicolás de los Garza, N.L., Mexico

<sup>c</sup> Instituto de Catálisis y Petroleoquímica, CSIC, c/Marie Curie 2, Cantoblanco, 28049 Madrid, Spain

## ARTICLE INFO

### Article history:

Received 11 June 2010

Received in revised form 9 August 2010

Accepted 23 August 2010

Available online 29 September 2010

### Keywords:

CO oxidation

CO preferential oxidation

Mesoporous silica

HMS–Ce

HMS–Fe

HMS–Ti

Au catalysts

## ABSTRACT

The effect of the modification of HMS (hexagonal mesoporous silica) support with Fe<sup>3+</sup>, Ce<sup>4+</sup> or Ti<sup>4+</sup> ions on the physico-chemical and catalytic properties of mesoporous Au/HMS catalyst was evaluated in the preferential oxidation (PROX) of CO, in hydrogen-rich stream (50 vol.% H<sub>2</sub>) and in the total CO oxidation (TOX) reaction. The bare supports were prepared via neutral S<sup>0</sup>/I<sup>0</sup> templating route, employing one pot synthesis, whereas the supported gold catalysts were prepared by the deposition–precipitation method. The reduced and spent Au catalysts have been studied by different techniques such as N<sub>2</sub> physisorption, oxygen storage capacity (OSC), XRD, HRTEM, hydrogen chemisorption (by TPD–H<sub>2</sub>), DRS UV–vis, Mössbauer and XPS spectroscopic techniques. Among the catalysts studied, Au/HMS–Fe recorded the highest activity and stability for total CO oxidation. The XPS and DRS UV–vis data suggest that the active-sites configuration of this catalyst during this reaction could be small gold particles and ionic gold species stabilized by the support. The Au/HMS–Fe catalyst was also able to oxidize CO selectively in a hydrogen-rich gas mixture (PROX reaction) at a relevant temperature to hydrogen fuel cell applications ( $T_{50} = 83^\circ\text{C}$ ). Additionally, the Au/HMS–Fe sample recorded the lowest hydrogen oxidation (undesired reaction) during the CO–PROX reaction in excess hydrogen. From the catalyst activity–structure correlation, the main factors influencing the superior catalytic behaviour of this sample in the CO–PROX reaction are (i) its largest Au species surface exposure, as determined by XPS for the spent catalysts; (ii) the largest population of small Au particles, as determined by HRTEM for the freshly reduced samples; (iii) the large oxygen and hydrogen storage capacities, and (iv) the lowest deactivation by the formation of surface coke species, as determined by coke burning followed by TGA technique.

© 2010 Elsevier B.V. All rights reserved.

## 1. Introduction

Recently, the development of the proton-exchange membrane (PEM) fuel cells technology has stimulated research in all areas of hydrogen generation and anode tail gas combustion catalysts [1]. The principal aim is to efficiently use the fuel cell effluents (CO, H<sub>2</sub>, and CH<sub>4</sub>) to produce, via oxidation reactions, the necessary energy for the hydrogen generation reactors and to minimize CH<sub>4</sub> and CO emissions [1]. The former one is a much more powerful greenhouse gas than CO<sub>2</sub>, whereas small amounts of CO present in the H<sub>2</sub> streams poison the Pt electrocatalysts of PEM fuel cells [2]. Thereby, among different approaches undertaken for the CO elimination, preferential CO oxidation (PROX: CO + 1/2O<sub>2</sub> + H<sub>2</sub> → CO<sub>2</sub> + H<sub>2</sub>O) remains prominent, because its low-cost, effective, available method for reducing CO to a desired level (less than 50 ppm of CO) without excessive hydrogen consumption [3].

The catalyst formulation used for PROX reaction involves Pt, Pd or Ru metals loaded on high surface area supports [2 and references within]. However, these catalysts are characterized by operating at high temperature (about 200 °C), and also need high excess of oxygen for complete depletion of CO, with corresponding lack of selectivity. The challenge is, therefore, to tailor novel catalysts that should oxidize 0.5–1% CO to less than 50 ppm at low temperature (near the operating temperature of the PEM fuel cells: 80–120 °C) without oxidizing a large amount of hydrogen [3,4].

Now then, since discovery of extremely fine gold nanoparticles with high activity in a low temperature CO oxidation [5,6], and of gold's catalysts reactivity in the reaction of hydrochlorination of ethylene to vinyl chloride [7], catalysis by gold is attracting rapidly growing interest [8 and references within]. The results are optimistic and gold has proved to be an effective catalyst for many reactions for which a catalyst had not been identified, e.g. for aromatics hydrogenation studied by us previously [9–11]. However, it is well known that gold catalysts are sensitive to the preparation conditions, gold particle size, and the metal–support interaction.

\* Corresponding author.

E-mail addresses: [trino@cny.unam.mx](mailto:trino@cny.unam.mx), [tzepeda@hotmail.com](mailto:tzepeda@hotmail.com) (T.A. Zepeda).

The gold particle size has a strong impact on the activity, because the reactivity of gold clusters depends largely on the type of uncoordinated sites exposed, ensemble effects and metal nanoparticles functionality, which can easily change during the reaction [12]. The influence of the catalyst's preparation method, support type, pre-treatment conditions, and Au particle size on the catalytic response of gold catalysts in CO oxidation was extensively reviewed by Bond and Thomson [13].

The gold-based catalysts also display variable catalytic activity, depending on the support [3]. This is because materials such as SiO<sub>2</sub>, Al<sub>2</sub>O<sub>3</sub> or MgO are considered to be “inert” supports, which do not participated in the reaction mechanism, whereas transition metal oxides such as Fe<sub>2</sub>O<sub>3</sub>, CeO<sub>2</sub> or TiO<sub>2</sub> are “active” in reaction due to their high oxygen storage capacity and well known catalytic and redox properties. Indeed, most investigators agree that high-activity gold catalysts can be supported on  $\alpha$ -Fe<sub>2</sub>O<sub>3</sub>, CeO<sub>2</sub> or TiO<sub>2</sub> materials [8 and references within]. Unfortunately, those reducible oxides have low specific area. As a consequence, the gold particles supported on pure Fe<sub>2</sub>O<sub>3</sub>, CeO<sub>2</sub> or TiO<sub>2</sub> are less stable than those supported on mixed oxide supports [14]. Thus, recently, the attempt was made for supporting gold catalysts on high surface area (ca. 500–1000 m<sup>2</sup> g<sup>−1</sup>) mesoporous silica materials such as MCM-48, HMS or SBA-15 [15–20]. In order to increase the oxygen mobility, those materials were modified with small amount of reducible metal oxide [18–20]. The chemical modification of mesoporous silica with transition metal oxides led to an increase of the activity in the total reaction of CO oxidation, as in the enhancement of catalyst thermal stability and in the minimization of Au particle sintering [21]. The positive effect of dispersing TiO<sub>2</sub> over silica on the stability of Au particles was ascribed in the literature to the inhibition, by development of Si–O–Ti linkages, of the anatase formation upon calcination [22,23]. Similar to the CO oxidation [18–20], the Au/Ti-SBA-15 systems showed an activity enhancement in the CO-PROX reaction compared to the Ti-free Au/SBA-15 [17].

Apart from the still unclear role of the support in CO oxidation, the nature of the active phase in supported gold catalysts remains controversial. Zanella et al. [24] compared a series of gold catalysts supported on calcined TiO<sub>2</sub> at different temperatures, and concluded that the catalytic activity for CO oxidation starts when metallic gold is formed. On the contrary, from XPS-activity correlation Park and Lee [25] concluded that oxidized gold species are more active than metallic gold. For the Au/Al<sub>2</sub>O<sub>3</sub> catalysts, an ensemble constituted by hydroxyl groups associated with Au<sup>+</sup> cation (Au<sup>+</sup>–OH<sup>−</sup>) and linked to Au<sup>0</sup> were suggested as active sites [26]. In line with this, it was recently reported that gold nano-sized particles, in a pure metallic state, exhibited a worse catalytic performance in low temperature CO oxidation on both Au/CeO<sub>2</sub> and Au/SiO<sub>2</sub>, in comparison with the cationic Au species [27]. It was concluded that the presence of non-metallic Au species could be the main requisite for the achievement of the highest CO conversion at low temperature. Likewise, the promoting role of Au<sup>+</sup> ions in CO oxidation was evident for Au/Ti-SBA-15 catalysts [20].

In the present work, we focus on the structural and electronic effects of HMS support modification with Fe<sup>3+</sup>, Ti<sup>4+</sup> and Ce<sup>4+</sup> cations on the performance of supported gold catalysts in the CO-PROX reaction in excess of hydrogen. Results are compared with those obtained from the CO oxidation (TOX) in the absence of hydrogen. To the best of our knowledge, neither the HMS material has been studied in the PROX reaction nor the effect of cation incorporation into this material has been reported to date. The chemical, structural and surface characterization of the samples was performed by means of different techniques, in order to elucidate the role of Au and cation introduced in the HMS in the selective oxidation of CO.

## 2. Experimental

### 2.1. Synthesis of HMS and metal-modified HMS supports

HMS was synthesized by a neutral S<sup>0</sup>I<sup>0</sup> templating route, as described by Tanev and Pinnavaia [28]. This method is based on hydrogen bonding and self-assembly between neutral primary amine surfactants, S<sup>0</sup> (dodecylamine 99%, Aldrich) and a neutral inorganic precursor, I<sup>0</sup> (tetraethylorthosilicate, 98% Aldrich). The iron(III) nitrate nonahydrate (Aldrich; 98%), tetrabutyl orthotitanate (Aldrich 98%) and cerium nitrate hexahydrate (Aldrich; 99%), were used as precursors of Ce, Fe and Ti modifying cations, respectively, with a Si/M (M = Ce, Fe, Ti) atomic ratio of 40 [29].

### 2.2. Catalyst preparation

The Au/HMS and Au/HMS–M (M = Ce, Fe, Ti) catalysts were prepared by the deposition–precipitation method described in detail previously [29]. Briefly, the support (2 g) was added to the appropriate amount of chloroauric acid solution in order to prepare catalysts with nominal Au loading of 3.5 wt.%. The mixture was vigorously stirred at 70 °C for 1.5 h to favour Au precursor diffusion into HMS pores. The solution was then cooled to room temperature, keeping the pH at 9.0 by the addition of a 5 M ammonia solution. The solids were washed twice with 1 M NH<sub>4</sub>OH solution and then several times with deionized water at room temperature. The catalysts were dried in air overnight at 90 °C and finally calcined in air at 280 °C for 1 h. The gold loading was determined by inductively coupled plasma atomic emission spectroscopy (ICP-AES).

### 2.3. Catalytic activity measurements

Both total CO oxidation and CO-PROX reactions were carried out in a fixed-bed quartz micro-reactor connected on-line to a GC Shimadzu 12-A with two packed columns (5-A and Porapack Q) equipped with a TCD, also a mass spectrometer (Hidden, HAL RC 301) was connected in line with the reactor outlet in order to track the evolved products. Each experiment used 0.3 g catalyst (particle diameter: 0.25–0.50 mm) mixed with 0.3 g glass beads (diameter 0.5 mm). The reaction temperature was measured by a Chromel–Alumel thermocouple placed in the middle of the catalyst bed.

#### 2.3.1. Total CO oxidation (TOX)

Catalyst activity in the total CO oxidation reaction was evaluated at atmospheric pressure in the 20–400 °C temperature range, with a heating rate of 3 °C min<sup>−1</sup>. Before the reaction, the catalysts were pre-treated *in situ* in flowing hydrogen (60 mL min<sup>−1</sup> at atmospheric pressure) at 300 °C for 2 h, and then the reactor was cooled to room temperature. The gas mixture containing 1 vol.% CO and 1 vol.% O<sub>2</sub> ( $\lambda = 2$ ) balanced with N<sub>2</sub> (total gas flow of 100 mL min<sup>−1</sup>). The parameter  $\lambda$  is defined as the amount of O<sub>2</sub> present in the gas mixture divided by the amount of O<sub>2</sub> needed to completely oxidize the CO in the feed [30]. The molar flow rate of the CO in this gas mixture was  $7.44 \times 10^{-7}$  mol s<sup>−1</sup>. The catalytic experiments were repeated several times in order to verify their reproducibility. Catalyst stability was evaluated in long-term (800 min) CO oxidation at 160 °C.

The catalytic performance was expressed in terms of  $T_{50}$  temperature, defined as the temperature at which 50% CO conversion was obtained. CO conversion ( $X_{CO}$ ) and catalyst deactivation ( $D$ ) were calculated from the following equations:

$$X_{CO} = \frac{[CO]_{in} - [CO]_{out}}{[CO]_{in}} \times 100 \quad (1)$$

$$D = \frac{X_{t=0} - X_{t=800}}{X_{t=0}} \times 100 \quad (2)$$

**Table 1**

Textural properties and low-angle XRD data of the pure supports.

Samples	$S_{\text{BET}}^a$ (m <sup>2</sup> /g)	$V_{\text{total}}^a$ (cm <sup>3</sup> /g)	$d^a$ (nm)	$d_{100}^b$ (nm)	$a_0^c$ (nm)	Wall thickness <sup>d</sup> (nm)
HMS–Fe	807	1.0	4.9	5.96	6.9	2.0
HMS–Ce	596	0.8	5.3	6.94	8.1	2.8
HMS–Ti	758	1.3	7.1	6.72	7.7	0.8
HMS	685	1.2	6.7	6.89	8.0	1.3

<sup>a</sup> Specific surface area ( $S_{\text{BET}}$ ), total pore volume ( $V_{\text{total}}$ ) and average pore diameter ( $d$ ).<sup>b</sup>  $d$ -spacing estimated from the X-ray patterns.<sup>c</sup> Unit cell parameter estimated from the position of the (100) diffraction line and calculated employing equation  $a_0 = d_{100} \times 2/\sqrt{3}$ .<sup>d</sup> Wall thickness obtained by subtracting pore size from the unit cell parameter.

where  $[\text{CO}]_{\text{in}}$  and  $[\text{CO}]_{\text{out}}$  are the inlet and outlet concentrations of CO, respectively;  $X_{t=0}$  and  $X_{t=800\text{ min}}$  are the CO conversions at time on-stream ( $t$ ) of 0 and 800 min, respectively.

Activities are also described in terms of the specific reaction rates calculated according to Eq. (3):

$$r = \frac{X_{\text{CO}} \cdot F_{\text{CO}}}{m_{\text{cat}}} \quad (3)$$

where  $r$  is the specific reaction rate [mol g<sub>cat</sub><sup>−1</sup> s<sup>−1</sup>],  $X_{\text{CO}}$  is CO conversion,  $F_{\text{CO}}$  is the molar flow rate of the CO (mol s<sup>−1</sup>) and  $m_{\text{cat}}$  is the catalyst weight (g). Since the amount of accessible metal cannot be precisely calculated, the activity was expressed in terms of total metallic sites (in mol<sub>CO</sub> g<sub>Au</sub><sup>−1</sup> s<sup>−1</sup>) calculated from the specific reaction rate taking into account the gold loading in the calcined samples (Table 2).

### 2.3.2. Preferential CO oxidation (PROX)

For the CO-PROX experiments, the catalysts were activated *in situ* in flowing hydrogen at 300 °C for 2 h. The catalysts were tested in the 30–320 °C temperature range, with a ramp rate of 2 °C min<sup>−1</sup>, under 2.8 bar of total pressure. The gas mixture containing 0.5 vol.% CO, 1.0 vol.% O<sub>2</sub> ( $\lambda = 4$ ), 50 vol.% H<sub>2</sub> and 48.5 vol.% N<sub>2</sub> was used with a total gas flow of 100 mL min<sup>−1</sup>. The molar flow rate of the CO in this gas mixture was  $3.72 \times 10^{-7}$  mol s<sup>−1</sup>. CO conversion and reaction rate were calculated using Eqs. (1) and (3), respectively. CO selectivity ( $S_{\text{CO}}$ ) was defined as follows:

$$S_{\text{CO}} = \frac{1}{2} \frac{(N_{\text{CO}_{\text{in}}} - N_{\text{CO}_{\text{out}}})}{(N_{\text{O}_{2\text{in}}} - N_{\text{O}_{2\text{out}}})} \times 100 \quad (4)$$

where  $N$  refers to moles of CO or O<sub>2</sub>.

## 2.4. Characterization techniques

### 2.4.1. N<sub>2</sub> adsorption–desorption isotherms

The textural properties of the bare supports were evaluated from the adsorption–desorption isotherms of nitrogen at −196 °C, recorded with a Micromeritics TriStar 3000 apparatus. The specific surface areas of the materials were calculated using the BET method within the 0.005–0.30 range of relative pressures ( $P/P_0$ ). Previously, the samples were degassed in vacuum at 270 °C for 5 h.

### 2.4.2. X-ray diffraction (XRD)

The bare supports and *ex situ* reduced catalysts (H<sub>2</sub> flow at 350 °C for 2 h) were characterized by powder X-ray diffractometry (step size 0.02°; 0.5 s) with a Philips X'Pert spectrometer, using Cu K $\alpha$  ( $\lambda = 0.15406$  nm) radiation. The assignment of the crystalline phases was based on JPDFS powder diffraction file cards. The gold crystal size was calculated from the most intense peak  $2\theta = 38^\circ$  using the Debye–Scherrer equation.

### 2.4.3. FTIR study of the framework vibration

Framework IR vibrations in the 4000–400 cm<sup>−1</sup> range were recorded using a Nicolet spectrophotometer working with a res-

olution of 4 cm<sup>−1</sup>. Wafers of the samples were prepared by diluting 2 mg of sample in 140 mg KBr and pressing at 0.7 MPa.

### 2.4.4. High resolution transmission electron microscopy (HRTEM)

The studies of the freshly reduced catalysts were carried out using a JEM 2100F microscope operating with a 200 kV accelerating voltage and fitted with an INCA X-sight (Oxford Instruments) energy dispersive X-ray microanalysis (EDX) system to verify the semi-quantitative composition of the supported phases. The fine powder of the *ex situ* reduced (5% H<sub>2</sub>/He, 350 °C, 1 h) catalysts was dispersed ultrasonically in hexane at room temperature. A drop of the suspension was placed on a lacey carbon-coated Cu grid. At least 10 representative images were taken for each sample. More than 250 particles were measured in order to obtain statistically reliable data of the particle size.

### 2.4.5. UV–vis diffuse reflectance spectra (DRS UV–vis)

UV–vis DRS of the oxide precursors, reduced and spent catalysts were recorded using a Cary 5E spectrophotometer (Varian) with a Praying Mantis cell in diffuse reflection mode equipped with a high temperature reaction chamber (Harrick Scientific) for *in situ* measurements.

### 2.4.6. Mössbauer spectroscopy

The Mössbauer measurements of the HMS–Fe support and reduced Au/HMS–Fe catalyst were performed in a CMTE model MA250 spectrometer at room temperature, using a <sup>57</sup>Co:Rh source moving in sinusoidal mode. Zero velocity was defined with respect to the centroid of the metallic iron spectrum using the  $\alpha$ -Fe as reference.

### 2.4.7. X-ray photoelectron spectroscopy (XPS)

X-ray photoelectron spectra of catalysts were measured in a RIBER LDM-32 apparatus provided with a hemispherical electron analyzer and an Mg K $\alpha$  ( $h\nu = 1253.6$  eV) X-ray source. The samples were placed in a copper holder over a sample-rod in the pre-treatment chamber, were degassed at 130 °C for 1 h at  $10^{-5}$  mbar and then transferred to the ion-pumped analysis chamber (residual pressure lower than  $7 \times 10^{-9}$  mbar). The binding energies (BE) were referenced to the C 1s peak (284.9 eV) to account for the charging effects. The areas of the peaks were computed after fitting the experimental spectra to Gaussian/Lorentzian curves and removing the background (Shirley function). Surface atomic ratios were calculated from the peak area ratios normalized by the corresponding atomic sensitivity factors.

### 2.4.8. Oxygen storage capacity (OSC)

The OSC measurements of the freshly reduced samples were carried out in a Micromeritics TPD/TPR 2900 apparatus. The reduction of the samples was carried out at 300 °C for 1 h, with a 10% H<sub>2</sub>/Ar flow (30 mL min<sup>−1</sup>). The OSC profiles were obtained by passing 1 mL of air (99.9% of purity) at 30 °C for 1 h. The amount of O<sub>2</sub> consumed was determined on line with a thermal conductivity detector (TCD).

#### 2.4.9. Hydrogen adsorption capacity

The hydrogen adsorption capacity of the freshly reduced catalysts was measured in a Micromeritics 2900 instrument equipped with a TCD. Prior to hydrogen adsorption, the sample (0.05 g) was reduced at 300 °C for 1 h (heating rate of 10 °C min<sup>-1</sup>) under a flow of 10 vol.% H<sub>2</sub>/Ar mixture (50 mL min<sup>-1</sup> of total flow), in order to have the same state of the catalyst gold species prior to CO oxidation reaction. After reduction, the catalyst was purged in a flow of argon (flow rate of 50 mL min<sup>-1</sup>) at 300 °C for 1 h and then cooled to room temperature. H<sub>2</sub>-adsorption was performed at room temperature for 1 h using 10 vol.% H<sub>2</sub>/Ar mixture (50 mL min<sup>-1</sup> of total flow), followed by catalyst purging with Ar flow at the same temperature for 1 h. Finally, the temperature-programmed desorption of adsorbed hydrogen (TPD-H<sub>2</sub>) experiments were conducted by heating the sample from room temperature to 1000 °C (10 °C min<sup>-1</sup>) under Ar flow.

#### 2.4.10. Thermogravimetric analysis (TGA)

The samples were characterized by temperature-programmed oxidation (TPO) followed by thermogravimetry (TGA/SDTA851 Mettler Toledo apparatus). Each sample (ca. 10 mg) was first heated to 200 °C for 1 h in N<sub>2</sub> (10 °C min<sup>-1</sup>; 200 mL min<sup>-1</sup>) to remove the volatile compounds. Once the sample had cooled to room temperature, the carbon deposited was burnt off by raising the sample temperature to a final temperature of 700 °C at a rate of 10 °C min<sup>-1</sup> in a 20% O<sub>2</sub>/N<sub>2</sub> gas mixture (50 mL min<sup>-1</sup>).

### 3. Results and discussion

#### 3.1. Characterization of supports and calcined catalysts

The hexagonal arrangement of all synthesized supports was confirmed by both the low-angle X-ray diffraction patterns (Fig. 1) and by the HRTEM technique (figures not shown here). For  $hkl=100$ , all supports record a prominent peak ca. 1.8°, characteristic of the HMS structure. HMS-Ti records the highest peak intensity, suggesting the best ordering of its mesopore structure in comparison with the other samples. The  $d_{100}$  spacing values are given in Table 1 along with the corresponding unit cell parameters ( $a_0$ ) and wall thickness values. It is noteworthy that the HMS support recorded a slight increase in the  $d$ -values and unit-cell parameter upon the incorporation of Ce<sup>4+</sup> cations. This is probably because of the larger size of Ce<sup>4+</sup> cation compared to Si<sup>4+</sup>.

The textural properties of the pure supports were evaluated from the N<sub>2</sub> adsorption–desorption isotherms. Specific area ( $S_{\text{BET}}$ ), total pore volume ( $V_{\text{tot}}$ ) and average pore diameter ( $d$ ) are shown in Table 1. The  $S_{\text{BET}}$  values follow the order: HMS-Fe > HMS-Ti > HMS > HMS-Ce, while the average pore diameter values follow the trend: HMS-Ti > HMS > HMS-Fe > HMS-Ce. Thus, the incorporation of Ti<sup>4+</sup>, Fe<sup>3+</sup> and Ce<sup>4+</sup> ions into HMS has multiple effects on the final textural properties of the samples, probably due to the nature of the precursors and the complex

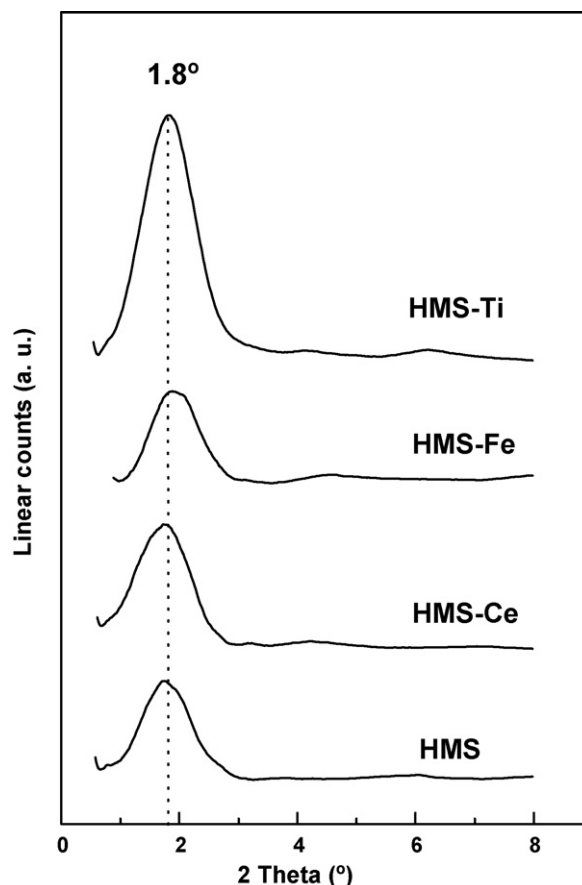


Fig. 1. Low-angle X-ray diffraction patterns of the pure supports.

assembling mechanism of the guest ions in the HMS framework. For HMS-Ce, the sharp decrease in surface area and average pore diameter suggests the partial deposition of ceria species in the HMS pores and/or pore blocking by those species.

The gold loading of the calcined catalysts (determined by ICP-AES) is reported in Table 2. From this table, the heteroatom loading (Fe<sup>3+</sup>, Ti<sup>4+</sup> and Ce<sup>4+</sup>) on HMS stabilizes the deposited gold maintaining higher loading in the Au/HMS-M catalysts than in the Au/HMS sample. Only traces of chlorine ions were detected. This is an important point, taking into account their high affinity to gold and high mobility on the support leading to agglomeration of supported Au particles during a heat treatment [31]. The normalized specific areas ( $NS_{\text{BET}}$ ) for all catalysts fall in the 0.59–0.78 range (see Table 2), indicating that Au particles are located mainly in the internal pore network of the support.

To summarise, the data obtained by different techniques shows that the majority of the ions become incorporated mainly into the HMS framework, principally in the Fe<sup>3+</sup> and Ti<sup>4+</sup> ions.

Table 2

Some characterization data of the HMS-based Au catalysts.

Support/catalyst	$NS_{\text{BET}}^a$	Au <sup>b</sup> (wt.%)	$d_{\text{Au}}^c$ (nm)	Population of Au particles <sup>d</sup> (%)	
				0.5–3 nm	3.5–6 nm
Au/HMS-Fe	0.59	2.84	4.6	90	10
Au/HMS-Ce	0.67	3.44	7.4	18	58
Au/HMS-Ti	0.74	3.02	5.2	70	30
Au/HMS	0.78	2.24	6.3	55	39

<sup>a</sup> Determined by N<sub>2</sub> physisorption at –196 °C for the calcined catalysts:  $NS_{\text{BET}}$ : normalized  $S_{\text{BET}}$  calculated from equation  $NS_{\text{BET}} = (S_{\text{BET}} \text{ of oxide catalyst}) / [(1 - y) \times S_{\text{BET}} \text{ of their respective support}]$ , where  $y$  is the Au loading determined by chemical analysis (ICP).

<sup>b</sup> Au loading determined by ICP technique.

<sup>c</sup> Au crystal size determined by XRD for the catalysts reduced in H<sub>2</sub> (300 °C, 2 h) and calculated using Debye–Scherrer equation for line at  $2\theta = 38^\circ$ .

<sup>d</sup> Determined by HRTEM for the catalysts reduced in H<sub>2</sub> (300 °C; 2 h).



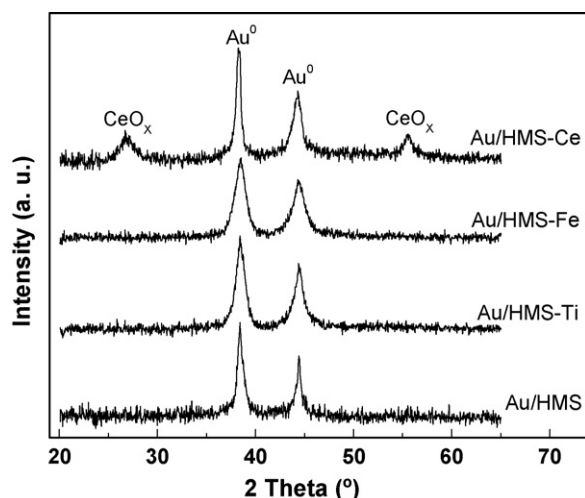


Fig. 2. Wide-angle XRD patterns of the freshly reduced HMS-based Au catalysts.

### 3.2. Characterization of the reduced catalysts

The presence of crystal phases in the reduced catalysts has been monitored by wide-angle X-ray diffraction measurements (Fig. 2). All freshly reduced catalysts record peaks at  $2\theta$  values at approximately  $38^\circ$  and  $44^\circ$ , characteristics of [111] and [200] planes,

respectively, which are attributed to metallic Au crystals [32]. The average particle size from XRD patterns is shown in Table 2. The Au crystal size calculated by the Debye–Scherrer equation to the XRD line at  $2\theta = 38^\circ$  follows the trend: Au/HMS–Ce (7.4 nm) > Au/HMS (6.3 nm) > Au/HMS–Ti (5.2 nm) > Au/HMS–Fe (4.6 nm). Thus, iron loading leads to an enhancement of gold dispersion. Besides the worst gold dispersion on the HMS–Ce material, this sample records diffraction lines at  $2\theta$  values of approximately  $27^\circ$  and  $56^\circ$  originated by  $\text{CeO}_x$  crystallites [33]. The formation of some fraction of  $\text{CeO}_x$  species blocking the support pores was also inferred from the  $\text{N}_2$  physisorption data (*vide supra*). On the other hand, the reduced Au/HMS–Fe and Au/HMS–Ti catalysts do not record any diffraction lines belonging to  $\text{FeO}_x$  and  $\text{TiO}_2$  moieties, respectively.

The morphology of the freshly reduced samples was examined by HRTEM (Fig. 3). This technique provides information on the real size and distribution of gold particles rendering it possible to observe the particles with sizes lower than the detection limit of XRD. The micrographs of all catalysts showed nearly spherically shaped Au nanoparticles. The statistical HRTEM analysis of the freshly reduced catalysts (Table 2) matches up with the XRD results (Fig. 2). The Au/HMS–Fe and Au/HMS–Ce had the largest and lowest population, respectively, of small Au particles (sizes in the 0.5–3 nm range) among the catalysts studied (Fig. 3). As was reported in Ref. [29], the average Au particle size follows the trend: Au/HMS–Ti ( $1.5 \pm 0.5$  nm) < Au/HMS ( $2.5 \pm 0.9$  nm) < Au/HMS–Fe ( $3.2 \pm 1.6$  nm) < Au/HMS–Ce ( $5.5 \pm 1.8$  nm). This trend did not match those of the Au particle size determined by XRD because

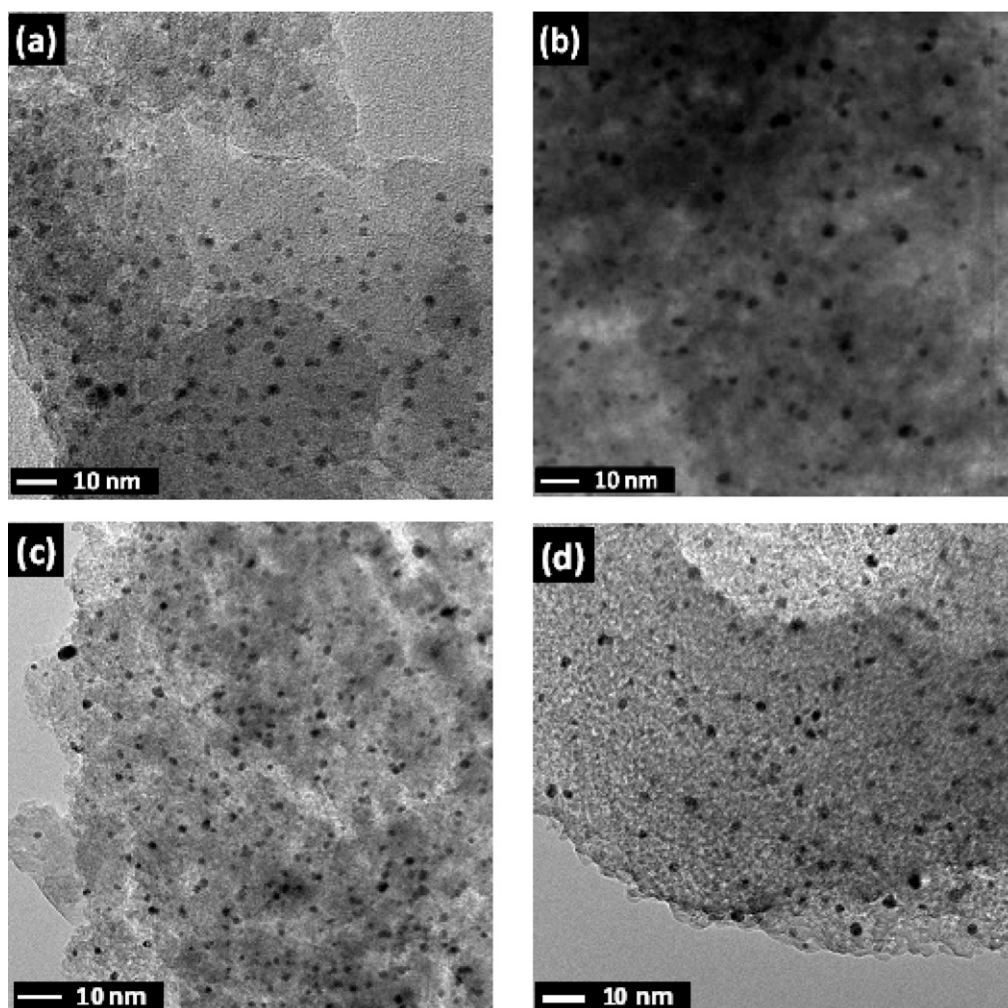
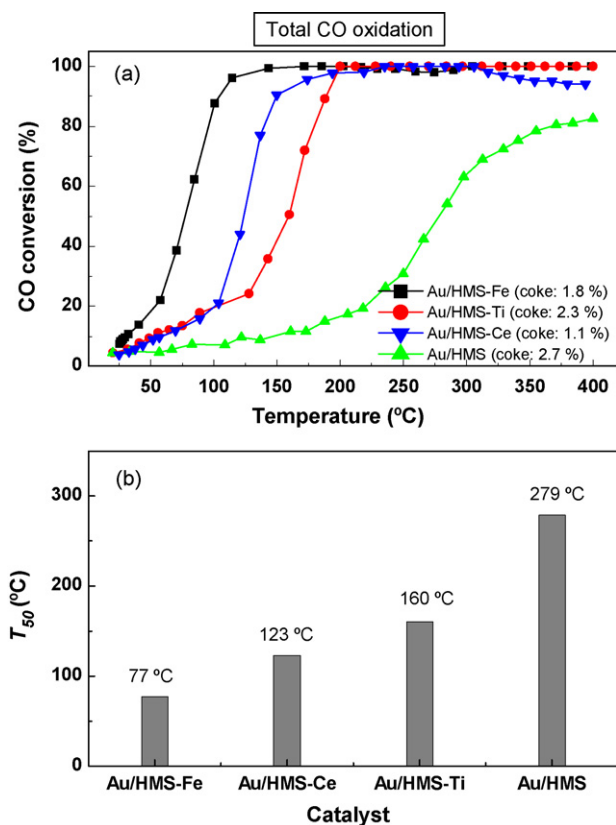


Fig. 3. HRTEM images of the freshly reduced HMS-based Au catalysts; Au/HMS (a); Au/HMS–Ce (b); Au/HMS–Fe (c); Au/HMS–Ti (d).



**Fig. 4.** (a) Variation in CO conversion with reaction temperature for total CO oxidation over the HMS-based Au catalysts ( $T = 20\text{--}400\text{ }^{\circ}\text{C}$ , 1 bar,  $\text{CO/O}_2/\text{N}_2 = 1/1/98\text{v/v}$ ,  $\lambda = 2$ ). Legend shows the amount of coke formed in the spent catalysts (by TPO/TG); (b) Comparison of the catalytic activities considering temperature at which 50% CO conversion was obtained ( $T_{50}$ ).

the latter technique cannot detect gold particles with a crystal size below 4 nm.

### 3.3. Catalytic behaviour in CO oxidation in the absence of $\text{H}_2$

To improve the catalytic activity of the Au/HMS catalyst, the effect of the support modification with  $\text{Ce}^{4+}$ ,  $\text{Fe}^{3+}$  and  $\text{Ti}^{4+}$  ions was investigated in the catalytic oxidation of CO in the  $20\text{--}400\text{ }^{\circ}\text{C}$  temperature range, with a total pressure of 1 bar, employing a gas mixture of  $\text{CO/O}_2/\text{N}_2$  (1/1/98v/v;  $\lambda = 2$ ). Before reaction, the catalysts were pre-treated under flowing hydrogen at  $300\text{ }^{\circ}\text{C}$  for 2 h. The support modification with  $\text{Ce}^{4+}$ ,  $\text{Fe}^{3+}$  and  $\text{Ti}^{4+}$  ions has a significant effect on CO conversion, as shown in Fig. 4(a). As seen in this figure, CO conversion increases with increasing reaction temperature, and all the samples recorded S-shaped profiles of CO conversion. Considering the temperature at which 50% CO conversion was obtained ( $T_{50}$ ), the activity trend was:  $\text{Au/HMS-Fe} > \text{Au/HMS-Ce} > \text{Au/HMS-Ti} \gg \text{Au/HMS}$  (Fig. 4(b)). The most active Au/HMS-Fe catalyst recorded the lowest  $T_{50}$  among the catalysts studied ( $77\text{ }^{\circ}\text{C}$ ).

Contrary to Au/HMS, CO conversions of 100% was obtained over Au/HMS-Ce, Au/HMS-Fe and Au/HMS-Ti catalysts (Fig. 4(a)). As compared to Au/HMS-Ce, the temperature at the maximum CO conversion of Au/HMS-Fe is shifted approximately  $50\text{ }^{\circ}\text{C}$  to a lower temperature ( $\sim 150\text{ }^{\circ}\text{C}$ ). More information could be obtained by considering the specific catalyst activities, expressed as moles of CO converted per gram of Au and per second. Thus, at a reaction temperature of  $80\text{ }^{\circ}\text{C}$ , the specific reaction rates follow the trend:  $\text{Au/HMS-Fe}$  ( $0.42\text{ mol}_{\text{CO}}\text{ g}_{\text{Au}}^{-1}\text{ s}^{-1}$ )  $>$   $\text{Au/HMS-Ce} \approx \text{Au/HMS-Ti} \approx \text{Au/HMS}$  ( $0.14\text{--}0.21\text{ mol}_{\text{CO}}\text{ g}_{\text{Au}}^{-1}\text{ s}^{-1}$ ).

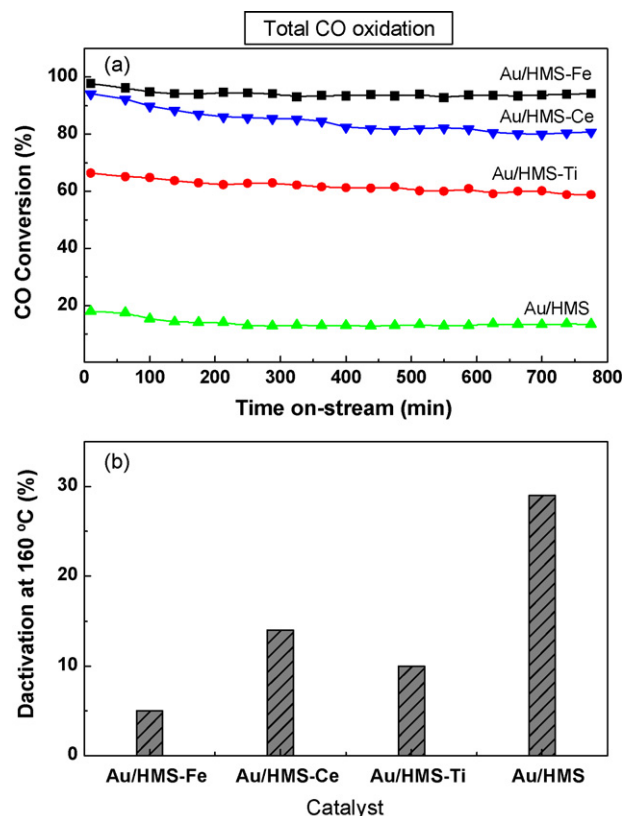


**Fig. 5.** (a) Long-term stability tests for total CO oxidation at  $160\text{ }^{\circ}\text{C}$  over the HMS-based Au catalysts. (b) Comparison of the catalyst's deactivation calculated using Eq. (2).

Thus, it was found that the Au/HMS-Fe sample has the highest specific activity among the catalysts studied.

Since catalyst deactivation by the  $\text{CO}_2$  formed is a common problem with gold catalysts [34], catalyst stability was evaluated in long-term (800 min) CO oxidation at  $160\text{ }^{\circ}\text{C}$  (Fig. 5(a)). The values of the catalyst deactivation calculated with Eq. (1) are compared in Fig. 5(b). As seen in this figure, catalyst deactivation with the reaction conditions used follows the order:  $\text{Au/HMS-Fe} < \text{Au/HMS-Ti} < \text{Au/HMS-Ce} < \text{Au/HMS}$ . The nature and extent of coke formation on these samples were studied by means of TG/DTG technique, measuring the weight loss of the coked catalysts upon temperature-programmed oxidation in  $20\text{ }^{\circ}\text{O}_2/\text{N}_2$  mixture (TGA profiles not shown here). Considering the weight loss of the spent samples during temperature-programmed oxidation in the  $200\text{--}700\text{ }^{\circ}\text{C}$  temperature range, the amount of surface coke species follows the trend:  $\text{Au/HMS-Ce}$  (1.1%)  $<$   $\text{Au/HMS-Fe}$  (1.8%)  $\sim$   $\text{Au/HMS-Ti}$  (2.3%)  $<$   $\text{Au/HMS}$  (2.7%). The confirmation of the surface coke species was obtained using the mass spectrometer on line with the oxidation reaction, tracking the  $\text{CO}_2$ , CO, and  $\text{O}_2$  signals. Thus, both the catalyst stability tests and the TPO/TGA results unambiguously indicated that support modification with cations enhanced catalyst stability, with Au/HMS-Fe being the most stable sample during on-stream conditions.

### 3.4. Catalytic behaviour in the CO-PROX reaction

The catalytic behaviour of the reduced Au catalysts was also studied in the CO-PROX reaction performed at 2.8 bar of total pressure in the temperature range between  $30$  and  $400\text{ }^{\circ}\text{C}$  with the composition of the gas mixture being  $\text{CO/O}_2/\text{H}_2/\text{N}_2 = 0.5/1/50/48.5\text{v/v}$  ( $\lambda = 4$ ). CO conversion, as a function of reaction temperature, is shown in Fig. 6(a). Similarly to total CO oxidation

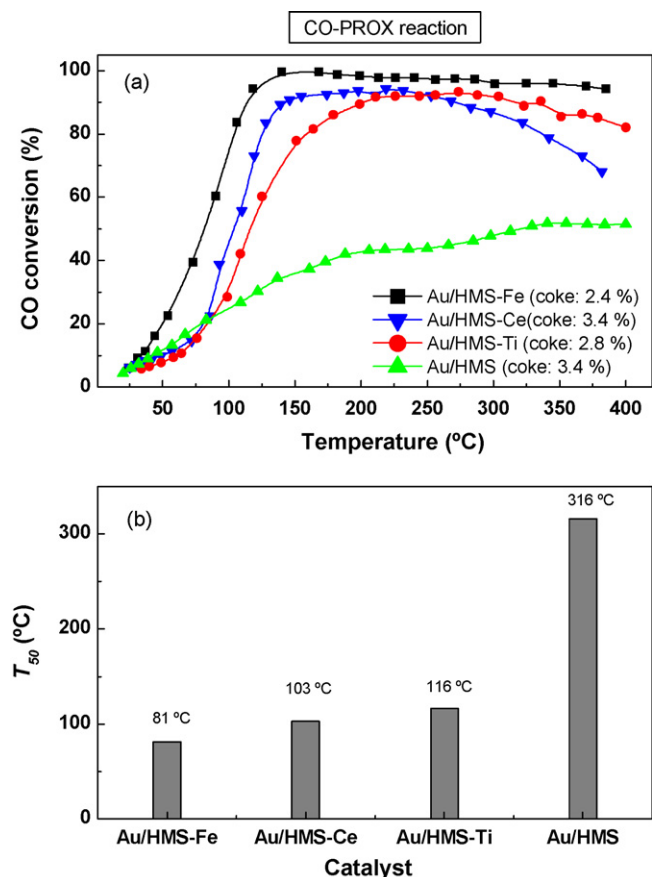


**Fig. 6.** (a) Variation in CO conversion with the reaction temperature for the CO-PROX reaction over the HMS-based Au catalysts ( $T=20\text{--}400\text{ }^{\circ}\text{C}$ ,  $P_{\text{total}}=2.8\text{ bar}$ ,  $\text{CO}/\text{O}_2/\text{H}_2/\text{N}_2=0.5/1/50/48.5\text{ v/v}$ ,  $\lambda=4$ ). Legend shows the amount of coke formed in the spent catalysts (measured by TPO/TG); (b) Comparison of the catalytic activities considering the temperature at which 50% CO conversion was obtained.

(*vide supra*), the highest activity in the CO-PROX reaction was achieved by the Au/HMS-Fe catalyst. Considering the activity trend at a reaction temperature of  $80\text{ }^{\circ}\text{C}$  ( $\text{Au/HMS-Fe}$  ( $0.93\text{ mol}_{\text{CO}}\text{ g}_{\text{Au}}^{-1}\text{ s}^{-1}$ )  $>$   $\text{Au/HMS-Ce} \approx \text{Au/HMS-Ti} \approx \text{Au/HMS}$  ( $0.14\text{--}0.24\text{ mol}_{\text{CO}}\text{ g}_{\text{Au}}^{-1}\text{ s}^{-1}$ ), it is obvious that the Au/HMS-Fe sample displays largest specific activity among the catalysts studied. Contrary to this sample, the Au/HMS-Ce, Au/HMS-Ti and Au/HMS catalysts do not reach 100% CO conversion under the reaction conditions studied. Fig. 6(b) shows the temperature at which 50% CO conversion was obtained ( $T_{50}$ ). As seen, the activity trend is similar to that observed for the catalysts tested in total CO oxidation ( $\text{Au/HMS-Fe} > \text{Au/HMS-Ce} > \text{Au/HMS-Ti} \gg \text{Au/HMS}$ ). However, a comparison of the specific rates at  $100\text{ }^{\circ}\text{C}$  indicated that the catalytic activities follow the trend:  $\text{Au/HMS-Fe} \gg \text{Au/HMS-Ce} \approx \text{Au/HMS-Ti} \approx \text{Au/HMS}$ . Thus, the Au/HMS-Fe catalyst recorded the highest specific activity in the CO-PROX reaction at the temperature relevant to hydrogen fuel cell application ( $T_{50}=81\text{ }^{\circ}\text{C}$ ). After reaching a maximum, the selectivity toward CO oxidation diminishes at temperatures above  $250\text{ }^{\circ}\text{C}$  for modified catalysts. Moreover, the Au/HMS-Fe sample recorded the lowest deactivation by forming coke species although, in this case, the produced amount of surface coke species on the PROX reaction was higher in comparison to the oxidation of CO, such as deduced from the burning of surface coke species followed by the TGA technique (see legend of Fig. 6(a)).

For all catalysts, the yields of products in reaction at  $375\text{ }^{\circ}\text{C}$  and 2.8 bars are compared in Fig. 7(a). For the Au/HMS and cation-modified catalysts, the reaction products originated in the CO-PROX

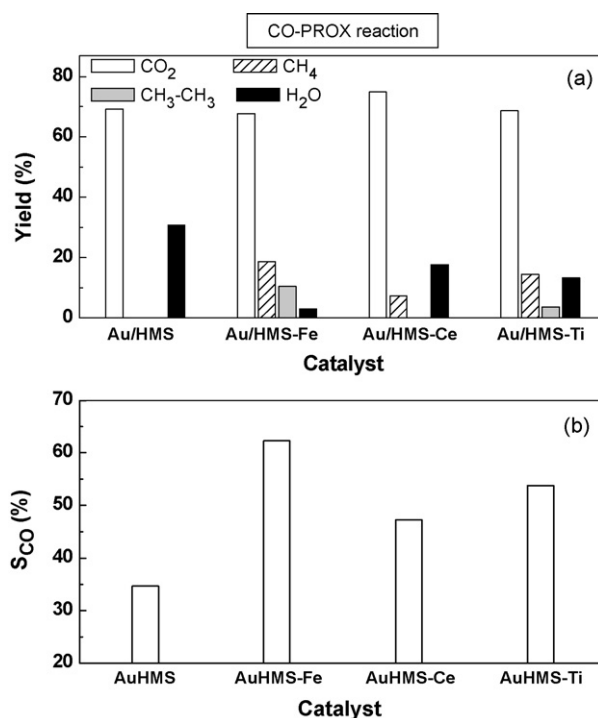


**Fig. 7.** CO-PROX reaction over HMS-based gold catalysts ( $T=375\text{ }^{\circ}\text{C}$ ,  $P_{\text{total}}=2.8\text{ bar}$ ,  $\text{CO}/\text{O}_2/\text{H}_2/\text{N}_2=0.5/1/50/48.5\text{ v/v}$ ,  $\lambda=4$ ): (a) yields of products; (b) CO selectivity; (c) CO conversion versus yield of  $\text{H}_2\text{O}$ .

reaction were different. The Au/HMS system showed the simplest selectivity, with the sole formation of  $\text{CO}_2$  and  $\text{H}_2\text{O}$  (75 and 25%, respectively). For the cation-modified catalysts, reaction products included  $\text{CO}_2$ ,  $\text{CH}_4$ ,  $\text{CH}_3\text{--CH}_3$  and  $\text{H}_2\text{O}$ . A higher yield of light hydrocarbons ( $\text{CH}_4$ ,  $\text{CH}_3\text{--CH}_3$ ,) and lower  $\text{CO}_2$  and  $\text{H}_2\text{O}$  formation were observed for the Au/HMS-Fe sample, followed by Au/HMS-Ti. The largest  $\text{CH}_3\text{--CH}_3$  and  $\text{CH}_4$  product formation in the PROX reaction over the Au/HMS-Fe sample (see Fig. 7(a)) confirmed the participation of hydrogen in the reaction mechanism. Considering the study by Bus et al. [35], the hydrogen could be dissociatively adsorbed on supported gold atoms, but such adsorption and dissociation is limited to the gold atoms on corner and edge positions. Additionally, molecular hydrogen could be adsorbed and dissociated on the under-coordinated Si atoms of the support [36].

In view of competitive CO and  $\text{H}_2$  oxidation, a target for the PROX reaction in excess  $\text{H}_2$  is to avoid the unwanted  $\text{H}_2 + 1/2\text{O}_2 \rightarrow \text{H}_2\text{O}$  reaction. Given that excess,  $\text{O}_2$  is needed for high CO conversion, in this study the oxygen factor ( $\lambda$ ) of 4 was employed ( $\text{O}_2/\text{CO}=4$ ). The selectivity for CO oxidation (CO selectivity) defined as the ratio of consumed CO to consumed  $\text{O}_2$  is shown in Fig. 7(b). Taking into account that competitive  $\text{H}_2$  oxidation increased with temperature, CO selectivity was determined at  $375\text{ }^{\circ}\text{C}$ . As seen in Fig. 7(b), CO selectivity follows the trend:  $\text{Au/HMS-Fe} > \text{Au/HMS-Ti} > \text{Au/HMS-Ce} > \text{Au/HMS}$ . Thus, the most active Au/HMS-Fe catalyst had the highest CO selectivity among the catalysts studied. For all catalysts, CO selectivity follows the trend:  $\text{Au/HMS-Fe} > \text{Au/HMS-Ti} > \text{Au/HMS-Ce} > \text{Au/HMS}$ . As expected, this trend is the same as that observed in the CO conversion versus the yield of  $\text{H}_2\text{O}$  formed (figure not shown here). The decrease in CO conversion with an increase in  $\text{H}_2\text{O}$  indicates that an unwanted  $\text{H}_2 + 1/2\text{O}_2 \rightarrow \text{H}_2\text{O}$  reaction occurs. The higher  $\text{H}_2\text{O}$  production during the catalytic performance of Au/HMS-Ce sample may have a negative effect in the overall activity toward the CO conversion, due to the competitive adsorption into the active sites between the CO and  $\text{H}_2\text{O}$  molecules [37].



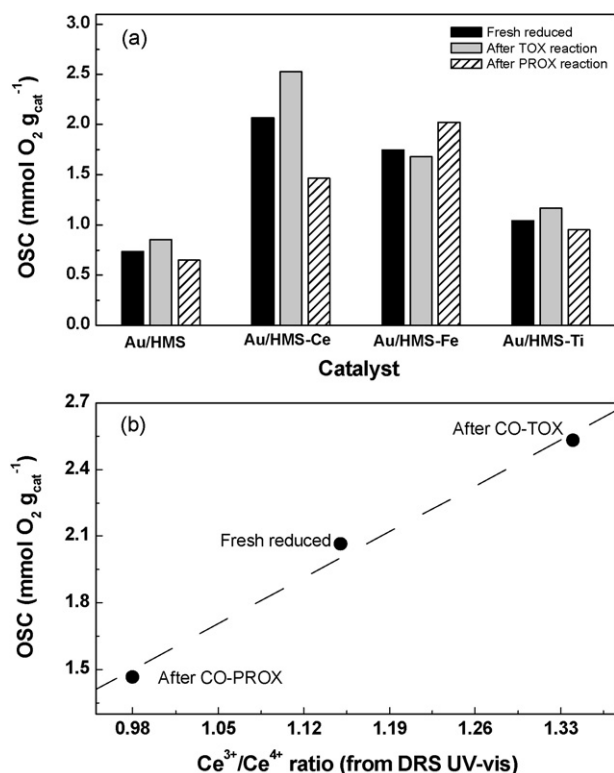


**Fig. 8.** (a) Comparison of the oxygen storage capacity (OSC) of the freshly reduced and spent samples tested in the total CO oxidation and CO-PROX reactions; (b) correlation between the Ce<sup>3+</sup>/Ce<sup>4+</sup> ratio of the reduced Au/HMS-Ce and the oxygen storage capacity of this sample before and after on-stream CO-TOX and CO-PROX reactions.

In short, for both total CO oxidation and CO-PROX reactions, the same catalytic activity trends were observed. Au/HMS-Fe recorded the best catalytic performance and highest stability in both reactions. For Au/HMS-Ce and Au/HMS-Ti, a slightly lower temperature was needed to achieve 50% CO conversion in the PROX reaction than in total CO oxidation in the absence of H<sub>2</sub>. Considering the study by Schumacher et al. [38], this is because the formation of carbonate-like species was inhibited on the surface of those catalysts in the presence of hydrogen.

### 3.5. Characterization of the spent catalysts

#### 3.5.1. Oxygen storage capacities

In order to study the possible participation of the support in the oxygen supply, the oxygen storage capacities of the freshly reduced and spent catalysts were investigated (Fig. 8(a)). The OSC of the freshly reduced and spent catalysts tested in the CO oxidation follow the trend: Au/HMS-Ce > Au/HMS-Fe > Au/HMS-Ti > Au/HMS, whereas those of the catalysts tested in the CO-PROX reaction were: Au/HMS-Fe > Au/HMS-Ce > Au/HMS-Ti > Au/HMS (Fig. 8(a)). In the case of the Au/HMS-Ce sample, it was observed (from the UV-vis spectra) that there is a linear correlation between the Ce<sup>3+</sup>/Ce<sup>4+</sup> ratio and the oxygen storage capacity of the freshly reduced and spent catalysts (Fig. 8(b)), suggesting that the oxygen adsorption capacity (OSC) of this sample depends on the Ce<sup>δ+</sup> environment promoted by a reducing or oxidizing atmosphere as will see below.

#### 3.5.2. UV-vis diffuse reflectance spectra

To compare the electronic variations undergone by the catalysts during the CO oxidation and CO-PROX reactions, the UV-vis diffuse reflectance spectra of the spent catalysts were compared with those of their freshly reduced counterparts. All spectra were recorded

at room temperature in the 200–900 nm range (Fig. 9(a)–(d)). As expected, all catalysts showed the plasmon resonance band, indicating the presence of metallic Au nanoparticles [29,39]. The plasmon resonance band is the effect of the collective oscillations of free conduction band electrons, induced by incident electromagnetic radiation when the wavelength of the incident light is greater than the particle size [40]. All freshly reduced samples displayed the plasmon resonance at ca. 2.1 eV, which accounts for the presence of Au-metallic nanoparticles on the catalysts. A higher intensity and broader band is recorded by the Au/HMS sample (Fig. 9(a)) indicating the higher reducibility of the Au supported on HMS. For the freshly reduced ion modified (Au/HMS-M) systems, the plasmon bands show similar intensities. The changes in the line-shape in the fresh solids are probably caused by differences in Au particle sizes supported on the different modified substrates (Table 2). The spent samples tested in both reactions show important changes in the intensity and shape of the plasmon resonance band. The changes were more notorious for the spent catalysts tested in the CO-PROX reaction.

Electronic spectra of the freshly reduced and spent Au/HMS-Ce samples are shown in Fig. 9(b). As seen in this figure, all UV-vis spectra show two absorption bands at ca. 3.8 and 4.7 eV (inset of Fig. 9(b)). The first signal at 3.8 eV is due to the oxygen-to-Ce<sup>4+</sup> charge transfer, while the band at 4.5 eV is associated with the oxygen-to-Ce<sup>3+</sup> charge transfer process [41]. As compared with the freshly reduced sample, the catalyst tested in total CO oxidation has a higher Ce<sup>3+</sup>/Ce<sup>4+</sup> ratio (1.15 versus 1.34) indicating that a fraction of Ce<sup>4+</sup> changes to Ce<sup>3+</sup> ions during on-stream conditions, which can be due to the loss of surface oxygen during CO oxidation. On the other hand, the spent catalyst tested in the CO-PROX reaction undergoes a slight decrease in the Ce<sup>3+</sup>/Ce<sup>4+</sup> ratio (from 1.15 to 0.98) indicating the oxidation of the surface Ce<sup>3+</sup> ions during on-stream reaction. All these changes can be explained considering that the oxidation of Ce<sup>3+</sup> ions is more thermodynamically favoured than the reduction of Ce<sup>4+</sup> ions, and that the Ce<sup>3+</sup> ions can be oxidized by oxygen atoms, which are produced in the reaction of CO hydrogenation to methane.

Electronic spectra of the freshly reduced and spent Au/HMS-Fe samples are shown in Fig. 9(c). The reduced Au/HMS-Fe recorded three important signals at ca. 2.6, 3.5 and 4.5 eV (see inset in Fig. 9(c)). The bands at 3.5 and 4.5 eV are commonly ascribed as due to oxygen-to-Fe<sup>3+</sup> charge transfer [42] whereas the band at 2.6 eV is generally associated with the presence of Fe<sup>2+</sup> cations, which are characteristic of small FeO<sub>x</sub> nanocrystallites [43]. Since the oxygen-to-Fe<sup>3+</sup> charge transfer seems to be more plausible than oxygen-to-Fe<sup>2+</sup> charge transfer, the electronic state of Fe ions in the pure HMS-Fe and reduced Au/HMS-Fe catalyst was clarified by Mössbauer spectroscopy (Fig. 10). The hyperfine Mössbauer parameters of the pure support and Au/HMS-Fe were: isomer shift ( $\delta$ ) values of  $0.31 \pm 0.05$  and  $0.33 \pm 0.05$  mm s<sup>-1</sup>, respectively, whereas those of the magnetic splitting ( $\Delta Q$ ) were  $0.86 \pm 0.05$  and  $0.89 \pm 0.05$  mm s<sup>-1</sup>, respectively. All parameters measured for both samples correspond only to species with Fe<sup>+3</sup> [44,45]. The small differences in the isomer splitting, and magnetic splitting values of the HMS-Fe and reduced Au/HMS-Fe samples are attributed to the presence of Au species in the latter sample. Therefore, the UV-vis band at 2.6 eV of the reduced Au/HMS-Fe catalyst could be attributed to the oxygen-to-Fe<sup>3+</sup> charge transfer. When comparing the DRS spectra of the spent Au/HMS-Fe catalyst with the freshly reduced one, there is an increase in the intensity of the absorption band at 2.6 eV. Additionally, the catalyst tested in CO oxidation has a small component at 3.5 eV, which could be associated with the oxygen enrichment of isolated Fe<sup>3+</sup> ions. Nevertheless, the small changes in the three electronic UV-vis spectra (freshly reduced Fe-catalyst and both spent catalysts) seem to prove that non-Fe leaching from HMS support occurs during on-stream reaction.



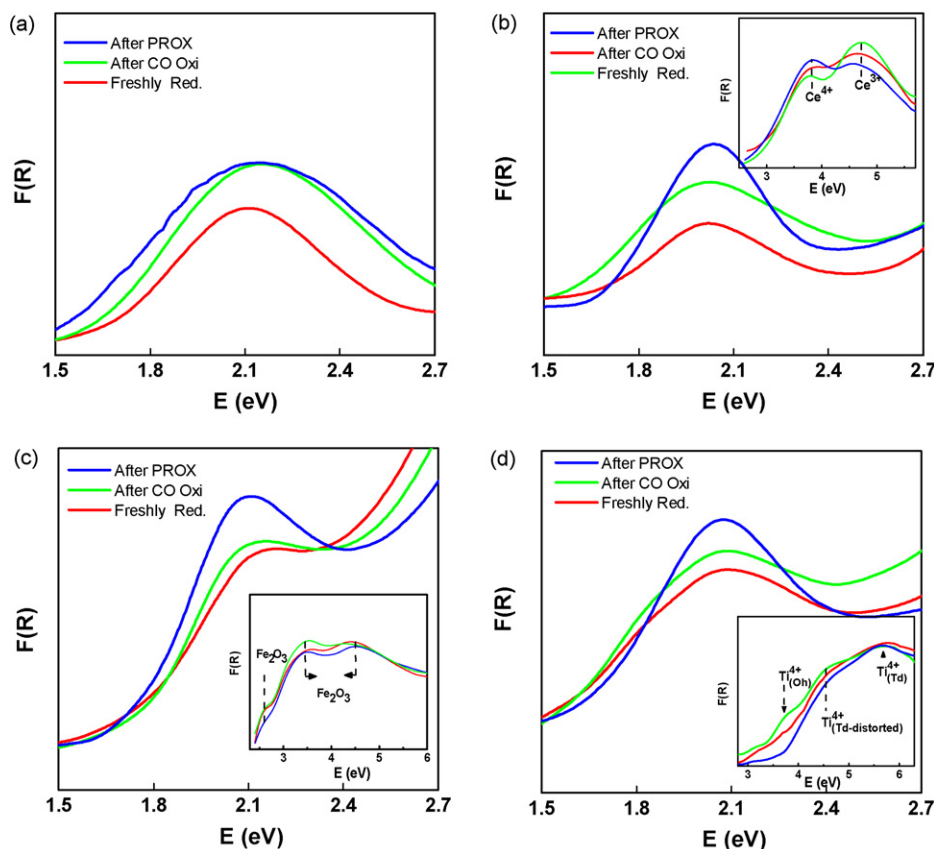


**Fig. 9.** Electronic spectra in the plasmon and doping zones (insets) of the freshly reduced and spent catalysts: (a) Au/HMS, (b) Au/HMS–Ce, Au/HMS–Fe (c) and Au/HMS–Ti (d).

The UV–vis spectrum of the freshly reduced Au/HMS–Ti sample is shown in the inset in Fig. 9(d). Two signals at ca. 4.6 and 5.7 eV can be observed, which are assigned to isolate tetrahedral and distorted-tetrahedral  $\text{Ti}^{4+}$  ions, respectively [46]. The catalyst tested in CO oxidation shows an additional band at 3.7 eV ascribed to the presence of octahedral  $\text{Ti}^{4+}$  ions [46]. The component at 5.7 eV is maintained with no changes, going from freshly reduced to spent catalyst tested in both CO oxidation and CO-PROX reactions. The catalyst tested in CO oxidation records an increase in the intensity of the band at 4.6 eV and an additional band at 3.7 eV. The last suggest that there is coarsening of Ti atoms, and the low

amount of Ti could be the reason of why this is not detected by DRX.

To summarise, a comparison between the UV–vis spectroscopy results of the spent Au/HMS–Ce and Au/HMS–Ti catalysts and those of their freshly reduced counterparts indicates that the coordination of  $\text{Ce}^{3+}/\text{Ce}^{4+}$  and  $\text{Ti}^{4+}$  ions undergoes major changes during on-stream conditions. On the one hand, Au/HMS–Ce shows some fraction of in the  $\text{Ce}^{4+}$  changes to  $\text{Ce}^{3+}$  ions during CO oxidation, whereas some oxidation of the  $\text{Ce}^{3+}$  to  $\text{Ce}^{4+}$  species occurs during the CO-PROX reaction. On the other hand, the Au/HMS–Ti catalyst tested in total CO oxidation records the formation of small  $\text{TiO}_2$  clusters on the support surface. By contrast, there is non-Fe leaching from the HMS support during on-stream CO-TOX and CO-PROX reactions over Au/HMS–Fe. This sample is unique, which shows an increase in the amount of metallic Au nanoparticles during the CO-PROX reaction, indicating the more difficult reduction in the gold species supported on the HMS–Fe substrate with respect to other catalysts. Thus, one might conclude that the Au/HMS–Fe sample has the largest metal–support interaction among the catalysts studied.

### 3.5.3. X-ray photoelectron spectroscopy

X-ray photoelectron spectroscopy analysis was used to determine the chemical state of elements and their surface proportions in spent catalysts. Fig. 11(a) and (b) shows the XP spectra of Au 4f core level of the catalysts tested in the total CO oxidation and CO-PROX reactions, respectively. The values of the binding energies (BE) of the Au 4f<sub>7/2</sub>, Ce 3d<sub>5/2</sub>, Fe 2p<sub>3/2</sub> and Ti 2p<sub>3/2</sub> are listed in Table 3 along with the Au/Si atomic ratios. For all catalysts, the Si 2p core level at 103.4 eV was observed. The Au 4f<sub>7/2</sub> binding energy found at  $83.8 \pm 0.1$  eV is typical of metallic Au particles [47]. The Au/HMS–Fe catalyst tested in CO oxidation shows an additional component at the lower BE value of 82.1 eV (Fig. 11(a)). Considering the HRTEM

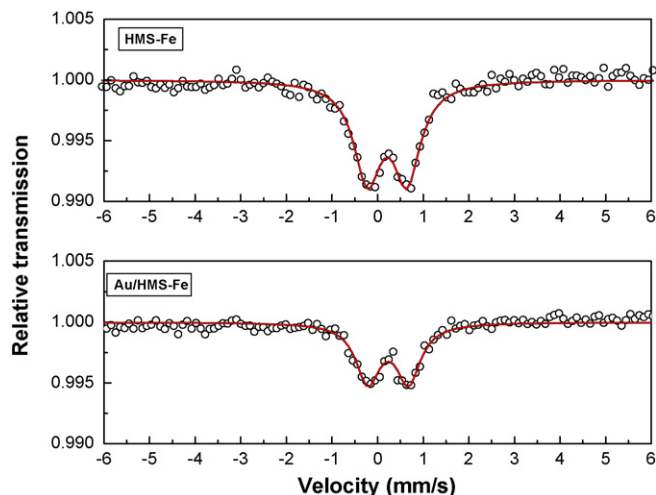


**Fig. 10.**  $^{57}\text{Fe}$  Mössbauer spectra of the HMS–Fe and reduced Au/HMS–Fe samples.

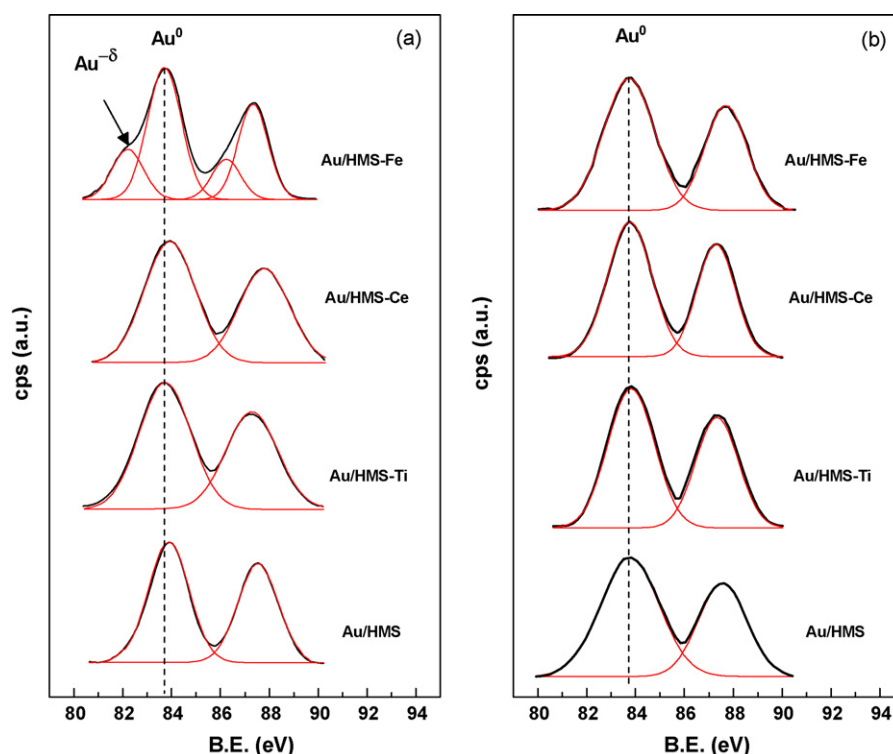


Fig. 11. Au 4f core-level spectra of the spent HMS-based Au catalysts tested in the CO-TOX (a) and CO-PROX (b) reactions.

(*vide supra*), this BE is due to small gold particles with an excess of electrons. In line with this, the Au/HMS-Fe tested in both CO oxidation and CO-PROX reactions has a BE at 710.9 and 710.6 eV, respectively (Table 3), indicating the presence of  $\text{Fe}^{3+}$  ions [48]. The lower value of BE (710.6 eV), obtained for the catalyst tested in the CO-PROX reaction, suggests some oxygen enrichment in the close proximity of the  $\text{Fe}^{3+}$  ions, which corroborates the DRS UV–vis and Mössbauer results.

The XP Ti  $2p_{3/2}$  spectra of the spent Au/HMS-Ti samples show two components with BEs at 460 eV and 458.5 eV. The high intensity component at 460.0 eV clearly indicates the presence of  $\text{Ti}^{4+}$  ions with a tetrahedral coordination [49], which is consistent with DRS UV–vis results. The minor Ti  $2p_{3/2}$  component at 458.5 eV is characteristic of titanium ions in an octahedral coordination [50]. For this catalyst tested in the total CO oxidation and CO-PROX reac-

tions, the amounts of octahedral Ti-O-Ti species (given in Table 3 in parentheses) were 25 and 20%, respectively. The higher amount of Ti octahedral in the catalyst tested in total CO oxidation suggests that some oxygen ions (from hydroxyl groups) are located in the coordination sphere of  $\text{Ti}^{4+}$  ions.

The XP spectra of Ce 3d core level of the spent Au/HMS-Ce catalysts show eight components, which correspond to the spin-orbit doublet and satellite lines characteristic of the Ce-oxidized state in agreement with the literature data [50]. The spin-orbit splitting is 18.4 eV, in accordance with the literature reports [51]. The Ce  $3d_{5/2}$  and  $3d_{3/2}$  showed the main components at ~882.4, 884.3, 892.5 and 898.5 eV corresponding to  $\nu$ ,  $\nu'$ ,  $\nu''$ ,  $\nu'''$ , respectively, and the components at ~902.2, 904.8, 907.4 and 916.8 correspond to  $u$ ,  $u'$ ,  $u''$  and  $u'''$ , respectively ( $\nu$  and  $u$  components in this study are in agreement with the report by Zou et al. [52]). The XPS

Table 3

Binding energies (eV) of core electrons and surface atomic ratios of the gold catalysts tested in CO oxidation in the absence (TOX)<sup>a</sup> and presence of hydrogen (PROX).<sup>b</sup>

Catalyst	Au 4f <sub>7/2</sub>		Ce 3d <sub>5/2</sub> (Fe 2p <sub>3/2</sub> or Ti 2p <sub>3/2</sub> )		Au/Si at	
	TOX	PROX	TOX	PROX	TOX	PROX
Au/HMS	83.9	83.7	–	–	0.0047	0.0044
	83.9	83.8			0.0052	0.0048
Au/HMS-Ce			882.4	882.5		
			884.2	884.3		
			892.6	892.4		
			898.5	898.4		
			902.2	902.2		
			904.9	904.8		
			907.3	907.4		
Au/HMS-Fe	83.7 (63)	83.8	710.9	710.6	0.0056	0.0058
	82.1 (37)					
Au/HMS-Ti	83.7	83.7	458.5 (25)	458.5 (20)	0.0049	0.0052
			460.0 (75)	460.0 (80)		

<sup>a</sup> Reaction conditions:  $P = 1$  bar;  $T = 20\text{--}400$  °C;  $\text{CO}/\text{O}_2/\text{N}_2 = 1/1/98\% \text{v/v}$ ;  $\lambda = 2$ .

<sup>b</sup> Reaction conditions:  $P_{\text{total}} = 2.8$  bar;  $T = 20\text{--}400$  °C;  $\text{CO}/\text{O}_2/\text{H}_2/\text{N}_2 = 0.5/1/50/48.5\% \text{v/v}$ ;  $\lambda = 4$ .

Ce-results reveal the presence of  $\text{Ce}^{4+}$  species, which are associated to  $u + u'' + u''' + v + v + v'''$  components, while the presence of  $\text{Ce}^{3+}$  species is deduced by the presence of  $u'$  and  $v'$  features [52]. Important changes in the  $\text{Ce}^{\delta+}$  environment were observed. The Au/HMS–Ce catalyst tested in total CO oxidation has a surface  $\text{Ce}^{3+}/\text{Ce}^{4+}$  atomic ratio of 0.37, whereas this sample tested in the CO-PROX reaction has a  $\text{Ce}^{\delta+}$  ratio of 0.29, in good agreement with the trend observed by the DRS UV–vis technique.

The surface Au/Si atomic ratios are listed in Table 3. For the catalysts tested in CO oxidation, the Au surface exposure follows the trend: Au/HMS–Fe > Au/HMS–Ce > Au/HMS–Ti > Au/HMS. This trend is a little different for the catalysts tested in the CO-PROX reaction (Au/HMS–Fe > Au/HMS–Ti > Au/HMS–Ce > Au/HMS). However, regardless of the reaction, the spent Au/HMS–Fe and Au/HMS catalysts showed the largest and lowest gold surface exposure, respectively, among the catalysts studied. Considering previously reported XPS results on the freshly reduced catalysts [29], the spent Au/HMS–Ce, Au/HMS–Fe and Au/HMS–Ti catalysts showed the enhancement of gold surface exposure with respect to their freshly reduced counterparts, indicating that during on-stream conditions there is some migration of the gold particles from the inner porous structure of the support to the support surface. The opposite process occurs with the Au/HMS catalyst, which shows some decrease in gold surface exposure after the on-stream reaction with respect to its freshly reduced form.

### 3.6. Correlation between catalytic activity and surface features

When considering catalyst performance in both the total CO oxidation and CO-PROX reactions, it is evident that the HMS support modification with  $\text{Ce}^{4+}$ ,  $\text{Fe}^{3+}$  and  $\text{Ti}^{4+}$  ions led to the enhancement of catalytic activity with respect to the Au/HMS sample, indicating the possible participation of the guest ions ( $\text{Fe}^{3+}$ ,  $\text{Ce}^{4+}$ , and  $\text{Ti}^{4+}$ ) in the reaction mechanism. Oxygen adsorption is therefore believed to occur at the metal–support interface region, possibly in the oxygen vacancies formed on the support [5,6]. The presence of  $\text{Au}^{\delta-}$  species in the spent Au/HMS–Fe catalyst (Table 3) suggests the presence of very small Au particles (Au-clusters) interacting strongly with the support, which occurs during on-stream conditions of the TOX reaction.

It is noteworthy, that catalysts tested in total CO oxidation show a correlation between the catalytic activity (by  $T_{50}$ ) with the oxygen storage capacity and Au species surface exposure in the spent catalysts (Fig. 12(a) and (b), respectively). The influence of the gold particle size is also deduced also from the correlation between catalytic activity and the population of gold clusters with sizes in the 0.5–3.0 nm range of the freshly reduced catalysts (Fig. 12(c)). This is because a decrease in the size of the supported particles results to an increase of the active phase surface area [53]. Thus, the superior catalytic behaviour of the Au/HMS–Fe catalyst in the total CO oxidation reaction can be explained by its highest oxygen storage capacity during on-stream conditions (see Fig. 8(a)), the largest Au species surface exposure, as determined by XPS for spent catalysts (Table 3) and the largest amount of small Au particles formed after catalyst reduction at 300 °C for 2 h, as determined by HRTEM (Table 2). Taking into account the XPS and DRS UV–vis data of the spent Au/HMS–Fe, it seems that the active-site configuration of this sample during total CO oxidation could be the small gold particles and ionic gold species stabilized by the support.

The Au/HMS–Ce catalyst is unique, recording a higher catalytic activity than is to be expected from its lowest population of small Au particles among the catalysts studied (Table 2), suggesting the possible “support effect”. Indeed, it is well known that ceria has high oxidation ability due to its high oxygen vacancies and low redox potential between  $\text{Ce}^{3+}$  and  $\text{Ce}^{4+}$  ions [41]. A comparison of the

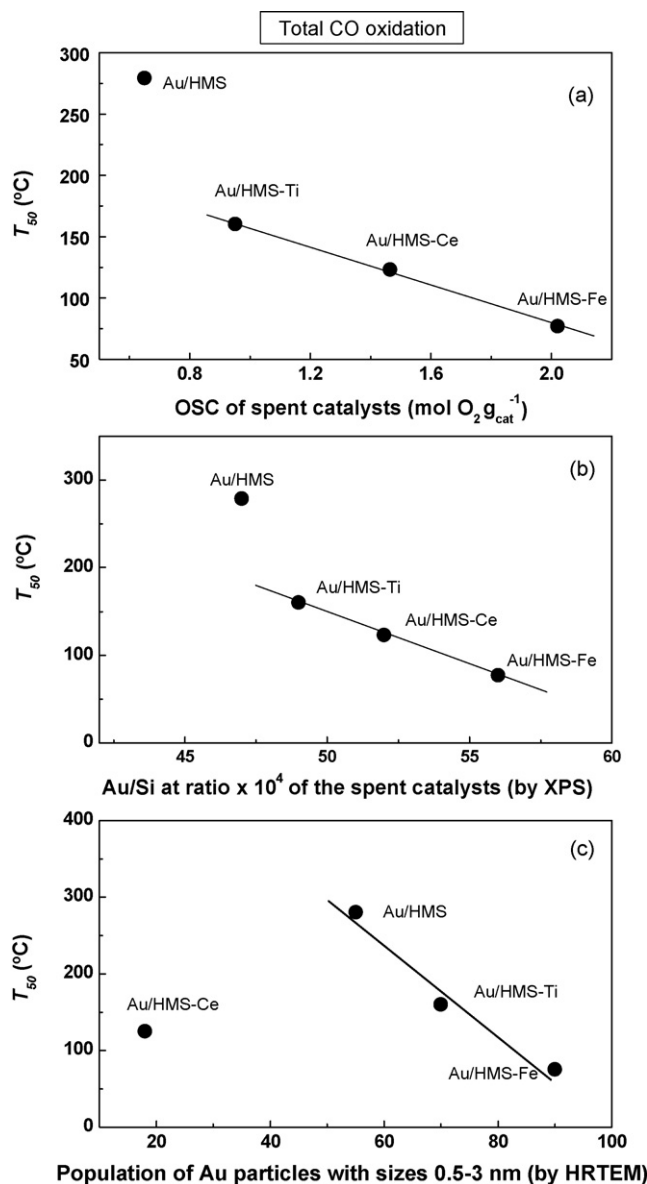


**Fig. 12.** Total CO oxidation over the HMS-based gold catalysts. Correlation between the catalytic activity (by  $T_{50}$ ) and the oxygen storage capacity: (a) Au species surface exposure (b) and the population of small-size gold clusters of the reduced catalysts (c).  $T_{50}$  – temperature at which 50% CO conversion was obtained.

oxygen storage capacity (OSC) values of the catalysts (Fig. 8(a)) indicates that the Au/HMS–Ce sample tested in total CO oxidation had the largest oxygen storage capacity among the catalysts studied, suggesting the support participated in the oxygen supply during the on-stream reaction. Thus, the catalytic response of Au/HMS–Ce sample in total CO oxidation is the sum of the positive effects of the large redox properties of the HMS–Ce material and, in the same way, the sample's highest oxygen storage capacity, which partially offsets the negative effect caused by the lowest population of small gold particles on the surface of this sample.

For the possible application in  $\text{H}_2$ –polymeric electrode fuel cells ( $\text{H}_2$ –PEMFCs), the catalyst should fulfil the following requirements: (i) be highly active in CO oxidation (in the case of  $\text{H}_2$ –PEMFC, be active in the 80–100 °C temperature range); (ii) show minimum activity in the undesired reaction of hydrogen oxidation; and (iii) be resistant towards deactivation by both  $\text{CO}_2$  and  $\text{H}_2\text{O}$  present in the feed [37]. In this work, the Au/HMS–Fe sample fulfils all those requirements. Considering the catalyst activity–structure correla-



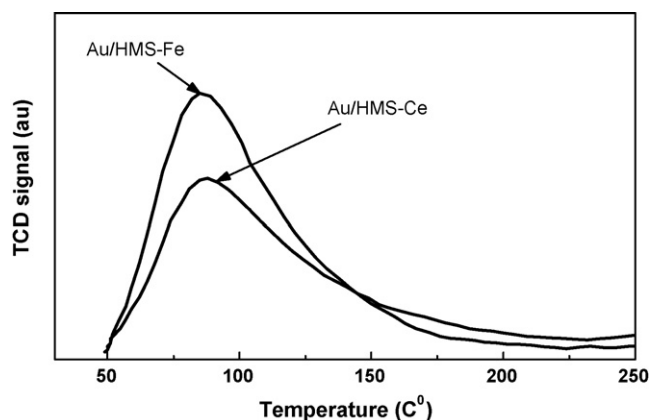


Fig. 13.  $H_2$ -TPD profiles of the freshly reduced Au/HMS–Ce and Au/HMS–Fe catalysts.

tion, the main factors influencing the superior catalytic behaviour of the Au/HMS–Fe sample in the CO–PROX reaction are (i) its largest Au species surface exposure, as determined by XPS (Table 3); (ii) probably to the largest population of small Au particles, as determined by HRTEM (Table 2); (iii) the large oxygen storage capacity; and (iv) the lowest catalyst deactivation by surface coke species, as determined by TGA technique.

Since the activity of the samples in the CO–PROX reaction could be related to the different hydrogen adsorption capacities of the samples, the hydrogen chemisorption experiments were performed on the two most active Au/HMS–Fe and Au/HMS–Ce catalysts pre-treated with pure  $H_2$  at 300 °C for 1 h. After hydrogen chemisorption, the samples were submitted to subsequent temperature-programmed desorption (TPD) in inert gas (Ar). The TPD– $H_2$  profiles of both the Au/HMS–Fe and Au/HMS–Ce catalysts are shown in Fig. 13 until 250 °C (temperature of the catalytic performance of the samples). The hydrogen desorption could be ascribed to hydrogen bonded to Au active sites. Considering the study by Bus et al. [35], the hydrogen is dissociatively adsorbed on supported gold atoms, but such adsorption and dissociation is limited to the gold atoms on corner and edge positions. Additionally, molecular hydrogen could be adsorbed and dissociated on the under-coordinated Si atoms of the support [36]. Depending on the reaction conditions, the large amount of hydrogen absorbed in the Au/HMS–Fe samples probably minimized the catalyst deactivation by the formation of surface carbonyls species, as confirmed by TPO/TGA experiments. Additionally, hydrogen could be directly involved in the reaction mechanism of the oxidation of CO, as the CO oxidation rate is enhanced before hydrogen starts to be oxidized [3]. Indeed, the largest  $CH_3$ – $CH_3$  and  $CH_4$  product formation in the PROX reaction over the Au/HMS–Fe sample could confirm the participation of hydrogen in the reaction mechanism. Then, the superior catalytic performance of the Au/HMS–Fe sample also could relate with the large hydrogen storage capacity of this sample.

#### 4. Conclusions

Several gold catalysts supported on hexagonal mesoporous materials modified with oxides of Ce, Ti and Fe were investigated for CO elimination by total oxidation and preferential oxidation (PROX) in a flow reactor system. On the basis of the data presented above, the following conclusions can be drawn:

- Regardless of the reaction and the oxide employed for support modification (Ce, Fe or Ti), the Au catalysts supported on HMS modified with different cations appeared to be more active and stable than the Au/HMS sample.

- The Au/HMS–Fe catalyst was most active in total CO oxidation, as well as being able to oxidize CO selectively in excess hydrogen at the temperature relevant to hydrogen fuel cell application ( $T_{50} = 80$  °C). Nevertheless, the catalytic performance of the Ti and Ce-containing samples could be relevant for this application.
- For the CO–PROX reaction, the superior activity of Au/HMS–Fe was explained in terms of (i) the highest oxygen storage capacity; (ii) to the largest Au surface exposure on the surface of this catalyst (by XPS and HRTEM); (iii) the lowest deactivation by surface coke species; and (iv) the largest  $CH_3$ – $CH_3$  and  $CH_4$  product formation. Both latter factors are linked with the large hydrogen storage capacity observed in this sample, as using TPD– $H_2$  experiments.

#### Acknowledgments

We would like to thank Prof. J.L.G. Fierro for his comments and suggestions. B.P. acknowledges the Comunidad de Madrid (CAM, Spain) for financial assistance to the project (S2009/ENE-1743). R.G.L. also thanks the Ministry of Science & Innovation, Spain (Ministerio de Ciencia e Innovación, España) for a “Ramón y Cajal” contract. Authors are grateful to Dr. M.A. Peña (CSIC, Spain) and Dr. M.G. Rosmaninho (UFMG, Brazil) for providing the TPO/TG and Mössbauer data, respectively. T.A. Zepeda wishes to express his gratitude to the CNYN-UNAM (Mexico).

#### References

- [1] I. Zacharaki, C.G. Kontoyannis, S. Boghosian, A. Lycourghiotis, Ch. Kordulis, *Catal. Today* 143 (2009) 38–44.
- [2] M. Navarro, M.A. Peña, J.L.G. Fierro, *Chem. Rev.* 107 (2007) 3952–3991.
- [3] E. Quinet, F. Morfin, F. Diehl, P. Avenier, V. Caps, J.-L. Rousset, *Appl. Catal. B: Environ.* 80 (2008) 195–201.
- [4] P. Panagiotopoulou, D.I. Kondarides, X.E. Verykios, *Appl. Catal. A: Gen.* 344 (2008) 45–54.
- [5] M. Haruta, T. Kobayashi, H. Sano, N. Yamada, *Chem. Lett.* 16 (1987) 405–408.
- [6] M. Haruta, N. Yamada, T. Kobayashi, S. Iijima, *J. Catal.* 115 (1989) 301–309.
- [7] G.J. Hutchings, *J. Catal.* 96 (1985) 292–295.
- [8] S.K. Hashmi, G.J. Hutchings, *Angew. Chem. Int. Ed.* 45 (2006) 7896–7936.
- [9] A.M. Venezia, V. La Parola, B. Pawelec, J.L.G. Fierro, *Appl. Catal. A: Gen.* 264 (2004) 43–51.
- [10] B. Pawelec, E. Cano-Serrano, J.M. Campos-Martin, R.M. Navarro, S. Thomas, J.L.G. Fierro, *Appl. Catal. A: Gen.* 275 (2004) 127–139.
- [11] B. Pawelec, A.M. Venezia, V. La Parola, S. Thomas, J.L.G. Fierro, *Appl. Catal. A: Gen.* 283 (2005) 165–175.
- [12] L. Barrio, P. Liu, J.A. Rodríguez, J.M. Campos-Martin, J.L.G. Fierro, *J. Phys. Chem. C* 111 (2007) 19001–19008.
- [13] G.C. Bond, D.T. Thompson, *Catal. Rev.: Sci. Eng.* 41 (1999) 319–388.
- [14] F. Moreau, G.C. Bond, B. van der Linden, B.A.A. Silberova, M. Makkee, *Appl. Catal. A: Gen.* 347 (2008) 208–215.
- [15] M. Bandyopadhyay, O. Korsak, M.W.E. van den Berg, W. Grünert, A. Birkner, W. Li, F. Schüth, H. Gies, *Micropor. Mesopor. Mater.* 89 (2006) 158–163.
- [16] A. Beck, A. Horváth, Gy. Stefler, R. Katona, O. Geszti, Gy. Tolnai, L.F. Liotta, L. Guzzi, *Catal. Today* 139 (2008) 180–187.
- [17] M. Ruszel, B. Grzybowska, M. Łaniecki, M. Wójcikowski, *Catal. Commun.* 8 (2007) 1284–1286.
- [18] J.A. Hernandez, S. Gómez, B. Pawelec, T.A. Zepeda, *Appl. Catal. B: Environ.* 89 (2009) 128–136.
- [19] L. Escamilla-Perea, R. Nava, B. Pawelec, M.G. Rosmaninho, C.L. Peza-Ledesma, J.L.G. Fierro, *Appl. Catal. A: Gen.* 381 (2010) 42–53.
- [20] C.L. Peza-Ledesma, L. Escamilla-Perea, R. Nava, B. Pawelec, J.L.G. Fierro, *Appl. Catal. A: Gen.* 375 (2010) 37–48.
- [21] R.J.H. Grisel, B.E. Nieuwenhuys, *Catal. Today* 64 (2001) 69–81.
- [22] G.J. Hutchings, *Catal. Today* 100 (2005) 55–61.
- [23] T.V. Choudhary, D.W. Goodman, *Top. Catal.* 21 (2002) 25–34.
- [24] R. Zanella, S. Giorgio, C.-H. Shin, C.R. Henry, C. Louis, *J. Catal.* 222 (2004) 357–367.
- [25] E.D. Park, J.S. Lee, *J. Catal.* 186 (1999) 1–11.
- [26] C.K. Costello, M.C. Kung, H.-S. Oh, K.H. Kung, *Appl. Catal. A: Gen.* 232 (2002) 159–168.
- [27] M.P. Casaletto, A. Longo, A.M. Venezia, A. Martorana, A. Prestianni, *Appl. Catal. A: Gen.* 302 (2006) 309–316.
- [28] P.T. Taney, T.J. Pinnavaia, *Science* 267 (1995) 865–867.
- [29] P. Castaño, T.A. Zepeda, B. Pawelec, M. Makkee, J.L.G. Fierro, *J. Catal.* 267 (2009) 30–39.
- [30] M.J. Kahlich, H.A. Gasteiger, R.J. Behm, *J. Catal.* 182 (1999) 430–440.
- [31] H.H. Kung, M.C. Kung, C.K. Costello, *J. Catal.* 216 (2003) 425–432.

- [32] P.X. Huang, F. Wu, B.L. Zhu, X.P. Gao, H.Y. Zhu, T.Y. Yan, W.P. Huang, S.H. Wu, D.Y. Song, *J. Phys. Chem. B* 109 (2005) 19169–19174.
- [33] Q. Fu, S. Kudriavtseva, H. Saltsburg, M. Flytzani Stephanopoulos, *Chem. Eng. J.* 93 (2003) 41–53.
- [34] S.D. Gardner, G.B. Hoflund, B.T. Upchurch, D.R. Schryer, E.J. Kielin, J. Schryer, *J. Catal.* 129 (1991) 114–120.
- [35] E. Bus, J.T. Miller, J.A. van Bokhoven, *J. Phys. Chem. B* 109 (2005) 14581–14587.
- [36] G. Zhao, W. Zhang, J. Sun, X. Shen, Y. Wang, *J. Mol. Struct.: THEOCHEM* 941 (2010) 71–77.
- [37] G. Avgouropoulos, T. Ioannides, Ch. Papadopoulou, J. Batista, S. Hocevar, H.K. Matralis, *Catal. Today* 75 (2002) 157–167.
- [38] B. Schumacher, Y. Denkwitz, V. Plzak, M. Kinne, R.J. Behm, *J. Catal.* 224 (2004) 449–462.
- [39] P. Claus, A. Brückner, C. Mohr, H. Hofmeister, *J. Am. Chem. Soc.* 122 (2000) 11430–11439.
- [40] R. Zanella, S. Giorgio, C.H. Shin, C.R. Henry, C. Louis, *J. Catal.* 222 (2004) 357–367.
- [41] Y.W. Zhang, R. Si, C.S. Liao, C.H. Yan, C.X. Xiao, Y. Kou, *J. Phys. Chem. B* 107 (2003) 10159–10167.
- [42] H. Liu, G. Lu, Y. Guo, Y. Guo, J. Wang, *Micropor. Mesopor. Mater.* 108 (2008) 56–64.
- [43] K. Bachari, J.M.M. Millet, P. Bonville, O. Cherifi, F. Figueras, *J. Catal.* 249 (2007) 52–58.
- [44] M.S. Batista, M.A. Morales, E. Baggio-Saitovich, E.A. Urquieta-Gonzalez, *Hyperfine Interact.* 134 (2001) 161–166.
- [45] E. de Grave, R.E. Vandenberghe, *Hyperfine Interact.* 28 (1986) 643–646.
- [46] T.A. Zepeda, J.L.G. Fierro, B. Pawelec, R. Nava, T. Klimova, G.A. Fuentes, T. Halachev, *Chem. Mater.* 17 (2005) 4062–4073.
- [47] A.M. Venezia, V. La Parola, G. Deganello, B. Pawelec, J.L.G. Fierro, *J. Catal.* 215 (2003) 317–325.
- [48] P. Reyes, H. Rojas, J.L.G. Fierro, *Appl. Catal. A: Gen.* 248 (2003) 59–65.
- [49] M.C. Capel-Sanchez, J.M. Campos-Martin, J.L.G. Fierro, M.P. de Frutos, A.P. Polo, *Chem. Commun.* (2000) 855–856.
- [50] P. Burroughs, A. Hamnett, A.F. Orchard, G. Thornton, *J. Chem. Soc., Dalton Trans.* 17 (1976) 1686–1698.
- [51] G.E. Arena, G. Centi, G. Deganello, L.F. Liotta, A. Macaluso, G. Pantaleo, *Top. Catal.* 30/31 (2004) 397–405.
- [52] Z.-Q. Zou, M. Meng, L.-H. Guo, Y.-Q. Zha, *J. Hazard. Mater.* 163 (2009) 835–842.
- [53] K. Bourikas, Ch. Kordulis, A. Lycourghiotis, *Catal. Rev.: Sci. Eng.* 48 (2006) 363–444.